Strong quantum turbulence in Bose-Einstein condensates

H. A. J. Middleton-Spencer,[1,2,*] A. D. G. Orozco,[3] L. Galantucci,[1,4] M. Moreno,[3] N. G. Parker,[1] L. A. Machado,[3] V. S. Bagnato,[3] and C. F. Barenghi[1]

[1]*Joint Quantum Centre Durham-Newcastle, School of Mathematics, Statistics and Physics, Newcastle University, Newcastle upon Tyne NE1 7RU, United Kingdom*

[2]*School of Physics and Astronomy, University of Birmingham, Edgbaston, Birmingham B15 2TT, United Kingdom*

[3]*Instituto de Física de São Carlos, Universidade de São Paulo, Av. Trabalhador São-carlense, 400 Pq. Arnold Schimidt, 13566-590 São Carlos, SP, Brazil*

[4]*Istituto per le Applicazioni del Calcolo "M. Picone," IAC-CNR, Via dei Taurini 19, 00185 Roma, Italy*

(Received 7 June 2022; accepted 11 July 2023; published 24 October 2023)

By combining experiments and numerical simulations which model the dynamics of shaken atomic Bose-Einstein condensates, we reveal the surprising nature of quantum turbulence in these systems. Unlike the tangles of vortex lines described in the superfluid helium literature, we find that our turbulent atomic condensate contains a mixture of strong fragmented density fluctuations and small random vortex loops which are not homogeneously distributed. This unusual form of turbulence, with its own properties and scaling behavior, which we call strong quantum turbulence, is significantly different from the turbulence which is observed in either classical or other quantum systems, thus posing a new challenge in turbulence research.

DOI: 10.1103/PhysRevResearch.5.043081

I. INTRODUCTION

Quantum fluids (e.g., superfluid helium, atomic Bose-Einstein condensates, polariton condensates, and the interior or neutron stars) differ from ordinary fluids in two respects. The first is superfluidity (the absence of viscosity), a consequence of the particular dispersion relation of elementary excitations. The second is more fundamental: the quantization of the circulation, a direct consequence of the existence of a macroscopic wave function describing the properties of the whole atomic cloud. This second property implies that vorticity is constrained to vortex lines of fixed strength, proportional to Planck's constant. Quantum turbulence (turbulence of a quantum fluid) thus consists of a disordered tangle of vortex lines moving over an inviscid background [1], unlike classical turbulence (turbulence of ordinary viscous fluids such as air or water) [2] where vortices are unconstrained in size and strength and are diffused by viscosity. Most work on quantum turbulence has been carried out in superfluid helium (both ^{4}He and ^{3}He), the driving concern being the comparison with classical turbulence. Indeed, dedicated cryogenic techniques to visualize vortex lines [3,4] and measure velocity fields [5–7] have led to the discovery of remarkable similarities between quantum turbulence and classical turbulence [8]. A major observed similarity [5,9] is the $k^{-5/3}$ Kolmogorov [10] energy spectrum (where k is the wave number) describing the distribution of kinetic energy over the length scales; this property is the signature of a universal effect: an energy cascade from large to small length scales. Further experiments have also uncovered nonclassical aspects of quantum turbulence [11–14] which still need to be understood. Unlike liquid helium, the properties of atomic condensates are exquisitely tunable, opening the possibility of studying the phenomenon of turbulence (still a major challenge for scientists) in a more general way. Unfortunately, the study of three-dimensional (3D) quantum turbulence in atomic condensates has been frustrated by difficulties in directly visualizing vortices and in measuring turbulent velocity fields (necessary to quantify intensity and structure of the turbulence); it is worth noticing that the absence of these difficulties in two-dimensional (2D) condensates has allowed great progress in 2D quantum turbulence [15–17]). Nevertheless, pioneering work with 3D condensates confined by harmonic traps [18] or boxtraps [19] has shown evidence of energy transfer from large to small length scales. However, attempts to observe the same scaling behavior measured in turbulent superfluid helium and in classical turbulence have not been successful, partly also due to the limited k-space available in atomic condensates given their small size. Our work tackles these difficulties. By combining experiments and numerical simulations which model the excitation of the condensate by shaking the confining external potential, we reveal that, surprisingly, turbulence in our atomic condensate is qualitatively different from the familiar tangles of vortex lines described in the superfluid helium literature and in previous numerical models of turbulent condensates [20,21], which in hindsight appear idealized. Instead, we find that the condensate contains huge nonlinear density waves, almost fragmenting the cloud. The vortex lines take the form of very short vortex loops, randomly oriented but distributed nonhomogeneously, instead of the familiar

*h.a.j.middleton-spencer@bham.ac.uk

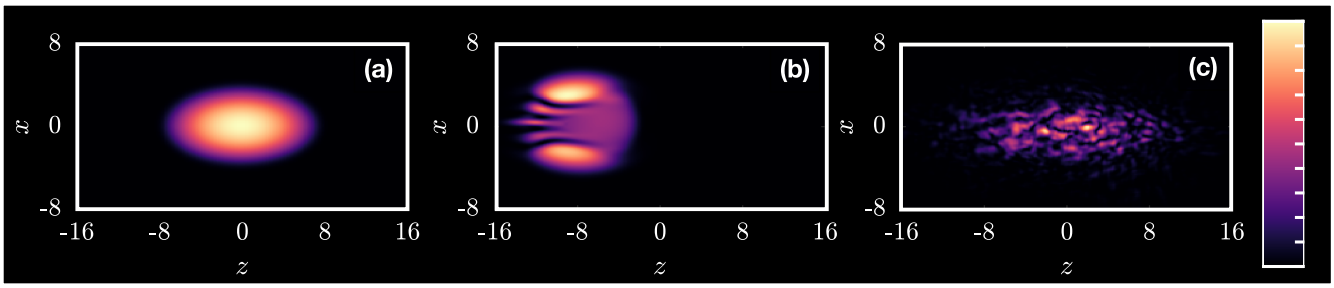

FIG. 1. 2D density slices $n(x, y = 0, z)$ of the simulated condensate at (a) $t = 0.0$ (the ground state), (b) $t = 4.9$ (nucleation of solitons), and (c) $t = 35.2$ (turbulent state with vortices and strong density waves).

distribution of long and short vortex lines observed in experiments and numerical simulations of turbulent helium. Such mixture of strong nonlinear waves and small random vortex loops nonhomogeneously distributed has never been reported in a turbulent system, either quantum or classical, and presents a new challenge in turbulent research.

II. EXCITING THE CONDENSATE

Various techniques to excite turbulence in condensates have been proposed, such as phase imprinting singly charged [21] or multicharged [22] vortices, or rotating the condensate [20,23]. Here we focus on the successful technique of shaking the trap confining the condensate [19,24]. This technique was first shown to create vortices [25–27] before being further developed in a number of notable studies revealing in particular the presence of a turbulent cascade [28]. In the experiment, we prepare a ^{87}Rb condensate of $N = 3 \times 10^5$ atoms within a cigar-shaped harmonic trapping potential (more details about experimental techniques in Appendix A and in Refs. [24–26]). The condensate is driven for a time T_D using a secondary oscillatory magnetic trap, followed by a waiting time T_H, in which the condensate is kept in the static harmonic trap, before finally released and imaged. In experiments, images of the condensate are typically taken from a light source which has traveled through the expanding condensate in the imaging plane after the trapping harmonic potential has been switched off. During the time-of-flight (TOF), the momentum distribution is obtained by observing the number of atoms traveling different distances from the beginning of the ballistic motion. Our group [29,30] and others [19] have demonstrated the validity of the TOF technique to obtain the 2D column-integrated momentum distribution $n(k)$ for a self-similar turbulent cloud.

III. COMPUTATIONAL METHODS

The experiment is simulated using the Gross–Pitaevskii equation (see Appendix B for details) nondimensionalized via harmonic-oscillator units as follows:

$$i\frac{\partial \Psi}{\partial t} = -\frac{1}{2}\nabla^2\Psi + \mathcal{C}|\Psi|^2\Psi + V\Psi - \mu\Psi. \tag{1}$$

The solution of Eq. (1) depends on two dimensionless parameters. The first parameter μ is the chemical potential, which dictates the size of the condensate. The second parameter ω_z appears in the axisymmetric trapping potential

$$V(x, y, z) = \tfrac{1}{2}\left[(x^2 + y^2) + \omega_z^2 z^2\right], \tag{2}$$

and sets the geometry (oblate, spherical, or prolate) of the condensate. The parameter $\mathcal{C}$, dependent on μ and ω_z, denotes the interaction strength (which in our case is positive, signifying repulsive interactions). For computational feasibility, we increase the experimental value of $\omega_z = 0.16$ to 0.5 and lower the chemical potential from $\mu = 13$ to $\mu = 8$. The parameter $\mathcal{C}$ is set to 1715 (see Appendix B). To generate turbulence we shake the condensate by superimposing an oscillatory potential of the form

$$V_{\rm osc}(x, y, z, t) = A\mu[1 - \cos(\Omega t)]z'/R_z, \tag{3}$$

to the harmonic trapping potential V, in Eq. (2), where A, Ω, and z'/R_z denote respectively the amplitude, the frequency and the length of the driving, R_z being the Thomas-Fermi radius in the z direction. We match the value of the amplitude A, frequency Ω, and time T_D to the experiment with $A = 1.25$, $\Omega = 0.97$, and $T_D = 10\pi/\Omega = 32.4$ (all values are reported in nondimensional units). The direction of the driving is $z' = \cos(\theta_z)z - \sin(\theta_z)x$ where $\theta_z = 5^\circ$ breaks the symmetry of the system around the z axis [24–26,31]. For $t > T_D$, the condensate is left to evolve and oscillate for T_H in the static harmonic potential [Eq. (2)].

IV. ONSET OF TURBULENCE

Figures 1(a)–1(c) show the shape of the condensate during the evolution, from the initial ground state, to the generation of deep density waves in the form of dark solitons, to the turbulent state, respectively. It is natural to ask what is nucleation process of vortex lines in the absence of an external, small-scale stirring potential ("laser spoon") [32,33]. The process is more clear during the first oscillation of the condensate, before it is masked by large density fluctuations. For a large driving amplitude ($A > 1$), dark solitons (nonlinear waves characterized by a localized dip in the density and a step in the condensate phase) appear at the front of the condensate moving in the $-z$ direction [Fig. 1(b)]. Solitons have previously been generated in condensates via a variety of techniques but are stable only in quasi-one-dimensional (quasi-1D) systems [34]. Indeed, the solitons quickly break down into vortex lines and sound waves [35], which respectively multiply and grow in size as the shaking continues [Fig. 1(c)]. For $t > T_D$, the condensate moves unforced and

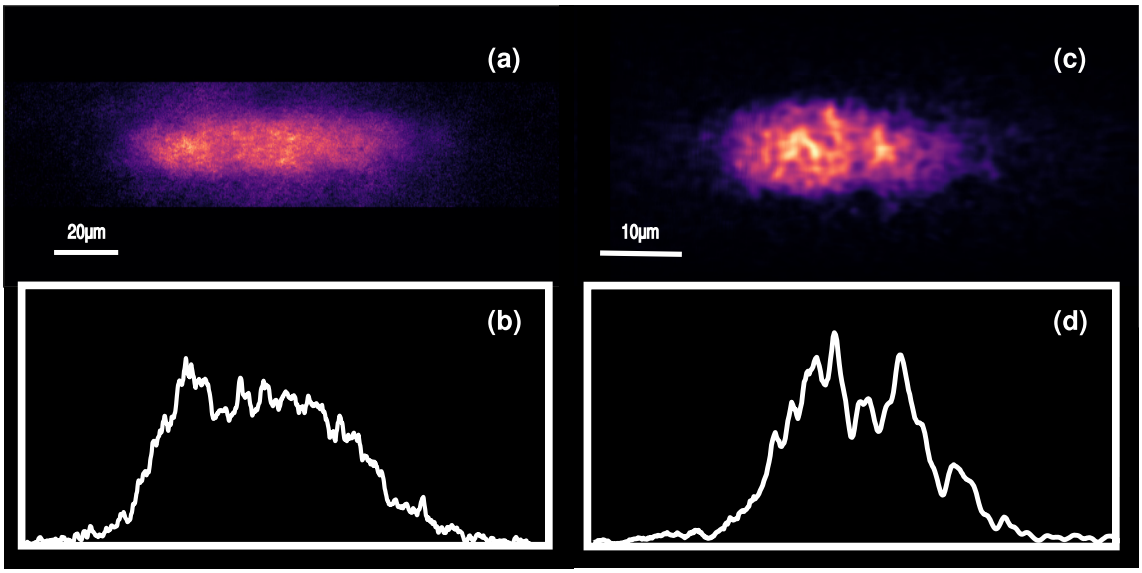

FIG. 2. Panel (a) shows an experimental absorption image of the turbulent condensate taken after a 30 ms TOF. Panel (c) shows the expanding computed 2D column-integrated density $n(x, z)$ (see Appendix B for details in the numerical expanded density). Panels (b) and (d) respectively correspond to experimental and numerical 1D slices of the integrated densities at $x = 0$, showing large fluctuations on top of a background density. Units of length, in SI form, are added to each TOF image for reference.

undergoes large oscillations about the minimum of the trapping potential, with a detectable breathing mode also present. During the oscillation, the condensate retains a shape similar to the initial cigar-shaped profile only when the center of mass is near the potential minimum at $z = 0$; it is most distorted when far from this minimum, near the points where the center of mass reverses its direction. The most notable features of the obtained turbulent state at $t > T_D$ are the observed large-density oscillations shown in Fig. 2, where experimental absorption images, necessarily 2D [Fig. 2(a)], are compared [Fig. 2(c)] to computed 2D column-integrated density fields $n(x, z)$, defined as

$$n(x, z) = \int |\Psi(x, y, z)|^2 dy. \tag{4}$$

To better appreciate the nonhomogeneous density characterizing the turbulent state, in Figs. 2(b) and 2(d) we also report the corresponding 1D density profiles.

V. MOMENTUM DISTRIBUTION

To characterize the turbulence we examine the momentum distribution $n(k)$ [29] where k is the magnitude of the wave number. Of particular interest here is the comparison with the momentum distribution obtained from experimental 2D density absorption images. For this purpose, we need to account for the expansion of the condensate. This is done by numerically simulating the expansion in the frame of reference of the center of mass after the trapping potential is set to zero. We compute the column integrated 2D density at different times t_{expan} after the beginning of the expansion of the turbulent BEC at $t = 66$, and, assuming ballistic expansion, we relate the position $\mathbf{x}$ on the enlarged condensate [18] to the wave number $\mathbf{k}$ of the atoms before the expansion; the final step consists of computing the momentum distribution $n(k)$. For simplicity and following the experimental procedure, we assume isotropy such that $k^2 = k_x^2 + k_z^2$. Although the time-of-flight expansion of the simulation is much smaller than that of the experiment, the spectra quickly converges to a power law in the k subrange of $k_{4\xi}$ to $k_{2\xi}$ (see Fig. 6 in Appendix B for the fittings of the exponents). The exponent of the power law quickly converges; taking the average of the results after $t = 68.0$ ($t_{\text{expan}} = 2.0$) (see Fig. 6), we obtain $n(k) \sim k^{-2.6\pm0.1}$ in the aforementioned range between $k_{a_0} = 2\pi/a_0$ (corresponding to the vortex core size $a_0 \approx 4\xi$) and $k_{2\xi} = 2\pi/2\xi$ (where ξ is the healing length). This distribution, shown in Fig. 3(a), compares well with the experimental distribution $n(k) \sim k^{-2.60}$ (obtained by averaging 10 experimental runs) shown in Fig. 3(b). This good agreement confirms the accurate modeling of the experiment, but it must be stressed that the range of wave numbers where the scaling takes place is narrow. This limitation arises from the small size of typical atomic condensates and prevents good quantitative comparison with turbulent superfluid helium and classical turbulence. In Fig. 3 we also report the momentum distribution of the expanded ground state which clearly shows how the excitation of the condensate has triggered an energy transfer towards small scales. In the next section, we show that large amplitude sound waves, fragmentation, and small vortex lines and loops are responsible for this incompressible energy transfer.

VI. VORTEX TANGLE

Besides large-density fluctuations and fragmentation, the turbulent condensate contains vortex lines, clearly visible in the numerical simulations. Surprisingly, the vortex configuration is very different from turbulence in superfluid helium.

We identify the vortex lines in the simulation using a vortex tracking algorithm established elsewhere for homogeneous or smoothly varying condensates [36–38]. In our

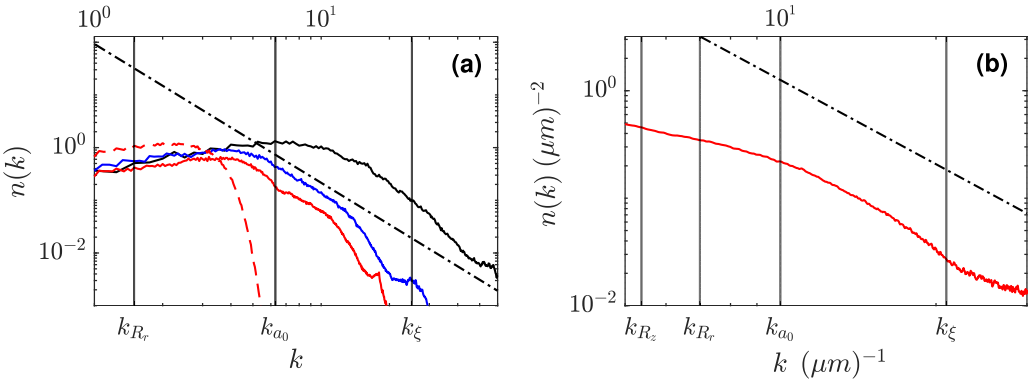

FIG. 3. The momentum distribution obtained from (a) an expanding numerical condensate released at $t = 66$ and (b) an average of 10 experimental images of the expanding turbulent state at an expansion time of 30 ms. The different distributions shown in panel (a) correspond to the expanding condensate at expansion times $t_{\text{expan}} = 0.5$ ($t = 66.5$) (black), $t_{\text{expan}} = 1.5$ ($t = 67.5$) (blue), and $t_{\text{expan}} = 2.5$ ($t = 68.5$) (red). For reference, the corresponding ground-state expansion at $t_{\text{expan}} = 2.5$ is given (red dashed). We show the early time expansion of $t_{\text{expan}} = 0.5$ to highlight the convergence in the later time results. The power-law fits, superimposed to each graph for reference, are $k^{-2.6}$ for both panels (a) and (b). Panel (b) is presented in SI units.

highly fragmented system, it is numerically challenging to identify vortices when the condensate is off-center in the trap (i.e., when the condensate is most fragmented and loses a discernible shape). We hence focus on vortex reconstruction when the condensate lies at the center of the trap.

The turbulent condensate and vortex lines therein at $t = 35.2$ is shown in Fig. 4. It is apparent that there are two kinds of vortex lines: small vortex rings (shown as blue lines in the figure) and short open vortex lines which terminate at the condensate's boundary (shown as red lines). These open vortex lines are shorter versions of the *U-shaped vortices* discussed in the literature of nonturbulent condensates [39–42]. Both vortex rings and U-vortices are small, of the order of the vortex core size a_0 (see Appendix C). The lack of homogeneity of the vortex configuration is immediately visible in the figure. Although just after T_D vortices are distributed more-or-less uniformly throughout the system, at later times most vortices reside at the back of the moving condensate (see Appendix D). When the longitudinal center of mass $\bar{z}$ is zero (Fig. 4), the vortex rings tend to be located along the central z axis of the condensate, while U-vortices tend to be more clustered towards the rear of the moving condensate which in Fig. 4 is moving toward the left. The orientation of the vortices, however, is fairly isotropic. The vortex length in each projected Cartesian direction falls between 30% and 40% of the total length at each time analyzed. It is therefore fair to conclude that in a turbulent condensate the vortex tangle is isotropic but not homogeneous. It is interesting to remark that, according to numerical simulations, small vortices have also been observed along the edges of a condensate excited by oscillating a box trap potential [19].

VII. ENERGY SPECTRUM

The current understanding of three-dimensional (3D) quantum turbulence in superfluid helium arises from combined experimental, numerical, and theoretical investigations [8] of the energy spectrum, $\hat{E}(k)$, defined by $E_i = \int_0^\infty \hat{E}(k)dk$ where k is the wave number and E_i is the total, incompressible, turbulent kinetic energy. The importance of $\hat{E}(k)$ is that it describes the energy distribution over the length scales, thus revealing interscale energy transfers. The key property of classical turbulence (described by the incompress-

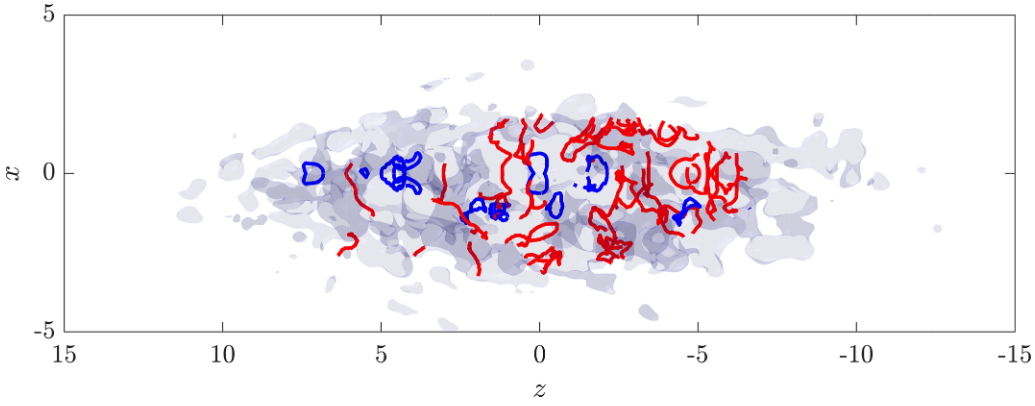

FIG. 4. The isosurface of the condensate at $t = 35.2$ with the central vortex lines marked. Line vortices are in red whereas ring vortices are in blue. Note that darker patches do not denote larger density but reveal the fragmented nature of the condensate because they result from the line of sight crossing the semitransparent density isosurfaces multiple times.

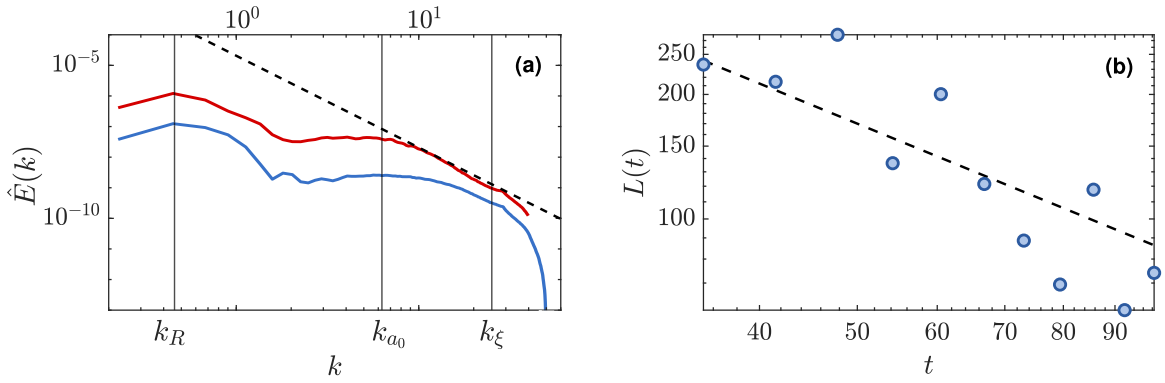

FIG. 5. (a) Numerical incompressible energy spectra $\hat{E}(k)$ of the condensate at times $t = 35.2$ (red) and $t = 92.0$ (blue). The dashed line, $\propto k^{-3}$, is drawn for reference. The spectra are shifted vertically for clarity. The vertical lines indicate the wave numbers k_R, and k_ξ corresponding in physical space to the longitudinal Thomas-Fermi radius $k_R = 2\pi/11 \approx 0.6$, and to the healing length ξ, respectively. The wave number k_{a_0} corresponds to the vortex width. (b) Total vortex line length $L(t)$ vs time t; the dashed line $\propto t^{-1}$ is given for reference.

ible Navier-Stokes equation) is the celebrated Kolmogorov scaling $\hat{E}(k) \sim k^{-5/3}$. In superfluid helium there appear to be two limiting regimes of quantum turbulence [12]: a *Kolmogorov regime* characterized by the same $\hat{E}(k) \sim k^{-5/3}$ observed in classical turbulence, indicating the existence of an energy cascade; and a *Vinen regime*, which is akin to a random flow, in which the energy spectrum peaks at the mesoscales Δ and decays as k^{-1} at length scales smaller than Δ and larger than the vortex core a_0. Unfortunately, the energy spectrum of turbulent 3D condensates is experimentally unavailable due to the lack of local velocity probes. There are also two significant differences with respect to liquid helium. First, condensates are very compressible and become easily fragmented (whereas the Kolmogorov scaling assumes constant density). Second, condensates are relatively small, so the spectrum extends only over a limited range of length scales, hindering any scaling law. In this respect, the comparison with liquid helium is staggering: the spatial extension of an atomic condensate is typically of the order of 10^2 times the size of a vortex core, whereas in helium experiments [43] the size of the system can be as high as 10^{10} vortex cores. To make progress, in our numerical part of the study, we obtain the energy spectrum $\hat{E}(k)$ of the turbulent condensate by extracting the incompressible kinetic-energy contribution, E_i, from the total kinetic energy via a standard Helmholtz decomposition [44]. The spectrum computed at two different times $t > T_D$ when $\bar{z} = 0$ is reported in Fig. 5(a), showing no significant temporal dependence. The wave number corresponding to the average radius of the vortices at $t = 35.2$, defined as $L/2\pi$ for vortex rings and L/π for U-shaped vortices is very close to k_{a_0}. In the range $1.5k_{a_0} \approx 10 < k < k_\xi \approx 25$ the energy spectrum scales approximately as k^{-3}, while no other scaling is observed at larger scales. At later times ($t = 92$) the average radius decreases with the range of the k^{-3} scaling decreasing accordingly. The k^{-3} scaling, in contrast to both Kolmogorov's and Vinen's spectra, directly stems from the small size of the vortices observed in our turbulent condensate. In fact, the k^{-3} spectrum reported between k_{a_0} and k_ξ coincides, as expected, with the incompressible kinetic-energy spectrum inside the core of a quantum vortex [44]. On the other hand, at smaller k, we lack the k^{-1} spectrum (which one would assume given the random orientation of the vortices [22]) precisely because the radii of the vortex rings are of the order of vortex core: there is no separation of scales between the radii of the vortex rings and their core, essential in order to observe the k^{-1} scaling, (see Appendix E). Indeed, if we compute the spectrum of a homogeneous gas of small vortex rings, we recover the same k^{-3} scaling for $k_{a_0} \lesssim k \lesssim k_\xi$, without further scalings at large scales (see Appendix E).

VIII. VORTEX DECAY

The random character of the vortex tangle is confirmed by the computed temporal decay of the total vortex length, which is itself a characteristic feature of the turbulent state. Indeed, by measuring the temporal behavior of the vortex length at all times when $\bar{z} = 0$, we find $L(t) \sim t^{-1\pm0.2}$ [Fig. 5(b)] matching the length temporal decay in the Vinen (random flow) regime, observed both in helium [11] and numerically in atomic condensates when the turbulence is created by the instability of antiparallel multicharged vortices [22]. This temporal decay behavior is clearly distinct from the $L(t) \sim t^{-3/2}$ decay observed in Kolmogorov superfluid helium turbulence [45–47].

IX. DISCUSSION

The regime of 3D quantum turbulence characterizing ongoing experiments on Bose-Einstein condensates excited via large-scale forcing [19,24] raises theoretical challenges. The turbulence which we have identified in our experimental and numerical study in fact reveals the presence of large-amplitude density waves, fragmentation, and a vortex tangle composed of very small, randomly oriented vortex loops and lines, nonhomogeneously distributed throughout the condensate. The small size of these vortical structures produces an incompressible energy spectrum exhibiting a k^{-3} scaling at small scales, stemming from the properties of quantum vortex cores [44], and lacking any additional scaling at large length scales, given the striking absence of long vortex lines (or even bundles of lines) which have been observed in experiments and numerical simulations of quantum turbulence in superfluid helium.

Overall, quantum turbulence generated in current experiments performed on confined condensates clearly appears to be distinct from the traditional turbulent regimes identified in other systems, i.e., Kolmogorov turbulence in both classical incompressible viscous fluids [2] and superfluid helium [8], Vinen turbulence in superfluid helium [11], and weak wave turbulence [48] in classical fluids (ocean waves, acoustic waves, etc.) and in quantum fluids (Kelvin waves on vortex lines [49,50]). None of these turbulence classes fully accounts for the turbulence observed in our study, which remarkably displays a coexistence of several turbulent features. In this perspective, the possibility of turbulence which combines vortex lines and weakly nonlinear density waves was indeed suggested years ago [51] for an idealized 2D homogeneous system. However, what we have found in an actual 3D turbulent atomic condensate is a more radical combination of unusually strong density waves and unusually small vortex loops ("unusual" in the sense of previous paradigms) which creates a scenario not seen in previous turbulence studies. This creates a window of opportunities to search for more possible phenomena that can only be present when different behavior coexist. This the important conclusion of this study. Future investigations should concentrate on the vortex nucleation mechanism, on how the turbulent features depend on the driving mechanism, and on the effect of thermal atoms.

This manuscript has associated data in a data repository. Additional metadata are available at Ref. [52].

ACKNOWLEDGMENTS

H.A.J.M.-S. thanks the Engineering and Physical Sciences Research Council of the UK (Grant No. EP/R51309X/1) for support. L.G., N.G.P., and C.F.B. acknowledges the Engineering and Physical Sciences Research Council of the UK (Grant No. EP/R005192/1) for support. L.G. acknowledges the support of Istituto Nazionale di Alta Matematica (Italy). A.D.G.O., M.M., L.A.M., and V.S.B. acknowledges financial support from FAPESP (Grant 2013/07276-1) and CNPq - Brazilian Agencies. This research made use of the Rocket High Performance Computing service at Newcastle University.

APPENDIX A: EXPERIMENTAL SETUP

A cloud of $N = 3 \times 10^5$ ^{87}Rb atoms is confined in a magneto-optical trap MOT1 cooled to around 140 μK and then transferred by radiation to a second magneto-optical trap MOT2, which captures, accumulates, and allows cooling to temperatures of a few μK. After this new entrapment and cooling, the optical fields are switched off, and the atoms are transferred to a magnetic trap composed of several coils forming a so-called IOFFE-PRITCHARD trap. Once in this trap, rf fields operating at a few MHz promote transitions causing the sample to evaporate. The loss of atoms during this phase is compensated by cooling, reaching temperatures of the order of 100 nK, where condensate begins and progresses, until we have a condensate fraction ranging from 50% to 80% of the total atoms. The condensate is trapped into a elongated harmonic potential with $\omega_z = 21 \times 2\pi$ rad/s and $\omega_r = 130 \times 2\pi$ rad/s.

Once the condensate has been successfully cooled within the final trap, a secondary oscillating magnetic field with $\omega_{exc} = 132.8 \times 2\pi$ rad/s is applied to the condensate. Here, a pair of anti-Helmholtz coils is applied close to the longitudinal axes of the static trap. The condensate is driven for a time of 37.65 ms, before the anti-Helmholtz coils are turned off and the system is left to evolve in the IOFFE-PRITCHARD trap. After T_H, the sample is allowed to expand freely for a period of 30 ms. At the end of this free-flight, a resonant probe laser takes an absorption image, revealing the 2D projection of the expanded density. This projection allows the extraction of the momentum distribution as well as the fluctuation profile. For more details on the measurements and experimental techniques we refer to Refs. [24–26].

APPENDIX B: NUMERICAL SIMULATIONS

At temperatures much lower than the critical temperature, an atomic condensate of N atoms with atomic mass m and scattering length a is quantitatively described by the Gross–Pitaevskii equation (GPE). It is convenient to rewrite the GPE in a dimensionless form using $\ell = [\hbar/(m\omega_r)]^{1/2}$ as the unit of length, $1/\omega_r$ as the unit of time, and N/ℓ^3 as the unit of the density $n = |\Psi|^2$, obtaining the dimensionless Gross–Pitaevskii equation (GPE) (1) and the normalization $\int |\Psi|^2 d\mathbf{x} = 1$. The parameters are chosen to match those of the experiment; the resulting dimensionless chemical potential and longitudinal trapping frequency are respectively $\mu = 13$ and $\omega_z = 0.16$. These values, combined with the large oscillation which is imposed to the condensate, would require a computational domain too large to simulate numerically. For this reason we increase the longitudinal trapping frequency to $\omega_z = 0.5$ and lower the chemical potential from $\mu = 13$ to $\mu = 8$. The dimensionless interaction parameter $\mathcal{C}$ is calculated assuming a Thomas-Fermi condensate so that $\mathcal{C} = \mu^{5/2}(16\pi\sqrt{2}/15)(1/\omega_z) = 1715$. The GPE is solved using finite differences on a 3D computational grid and fourth-order Runge-Kutta time integration. The mesh size and time step are $\Delta x = 0.125$ (corresponding to half of the system's healing

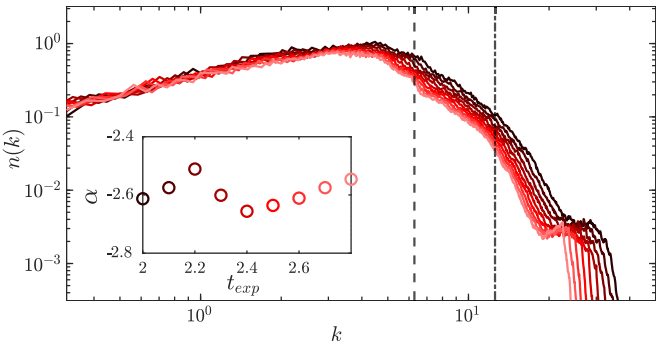

FIG. 6. The momentum distributions from $t_{\text{expan}} = 2.0$ to 2.8 ($t = 68.0$ to 68.8) (going from dark to light) with the boundaries of fitting marked by $k = 2\pi/4\xi$ (vertical dashed line) and $k = 2\pi/2\xi$ (vertical dot-dashed line) and (inset) the power exponents for each of the momentum spectra in the corresponding color.

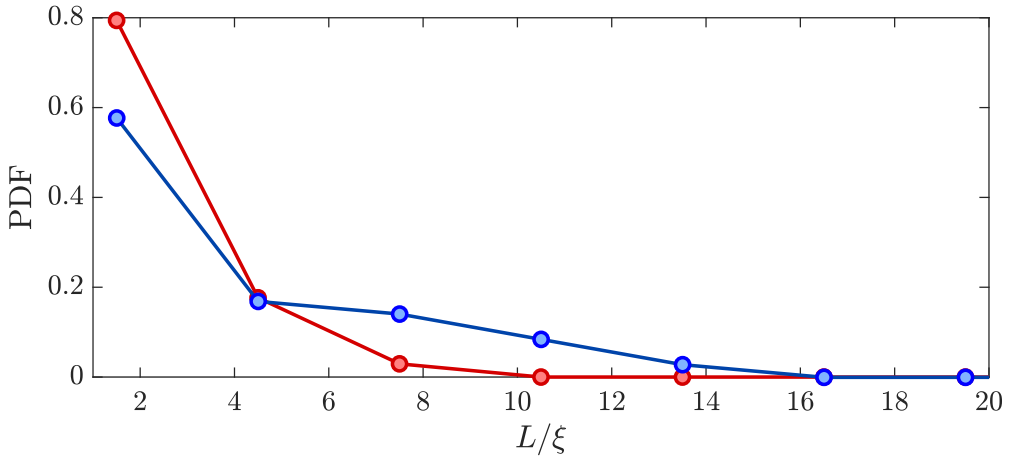

FIG. 7. The probability density function of the lengths (in healing length) of all individual vortices within the condensate at $t = 35.2$ (blue) and $t = 92.0$ (red).

length at the center of the trap) and $\Delta t = 0.001$, respectively. To find the initial ground state of the system, we first run the GPE in imaginary time, before moving to real time to observe the dynamics of the system with a total simulation time of $t = T_D + T_H = 100$. The method of obtaining the spectral exponent is shown in Fig. 6; the condensate is released at $t = 66.0$, at which it expands outwards and the momentum distribution is obtained. The condensate expands for a time t_{expan}, and an exponent α is obtained from fitting a power law between $k = 2\pi/4\xi$ and $k = 2\pi/2\xi$. The exponent measured in this interval quickly ($t_{\text{expan}} \geqslant 2.0$; $t \geqslant 68.0$) converges. Plotted in Fig. 6 are the results of the momentum distribution from $t_{\text{expan}} = 2.0$ to 2.8 ($t = 68.0$ to $t = 68.8$) with the inset providing the individual fitted power exponents obtained from each respective distribution in this k range. The reported power law in this paper is taken as the average of these nine exponents to give a result of $\alpha = -2.6 \pm 0.1$.

APPENDIX C: THE PROBABILITY DENSITY FUNCTION OF VORTEX RADII

The probability density functions of the length of individual vortex rings and U-vortices at times $t = 35.2$ and 92 are shown in Fig. 7. Here, the change of the vortex length towards smaller scales at later times is apparent as the PDF's width decreases.

APPENDIX D: ISOSURFACES OF THE TURBULENCE CONDENSATE IN TIME

Figure 8 displays vortex rings and U vortices as red lines together with the blue density isosurface of the condensate (in contrast, Fig. 4 of the main text differentiates between vortex rings and U vortices). At $t = 35.2$, in Fig. 8(a), the vortices are distributed almost uniformly in space. The condensate in Fig. 8(b) at $t = 60.5$ is traveling to the right of the figure, whereas Fig. 8(c) at $t = 92.0$ is moving to the left. Note that the vortices tend to be located in the back of the moving condensate.

APPENDIX E: INCOMPRESSIBLE ENERGY SPECTRA OF RINGS

It is known that the energy spectrum of a single straight vortex line of infinitesimal thickness in a fluid of constant density decays as k^{-1} for large k. If the vortex line is in the shape. If the vortex line is in the shape of a ring of radius R, the energy spectrum [53] rises as k^2 for small k, peaks at $kR \approx 1$, and decays as k^{-1} at larger k with characteristic small amplitude oscillations. A gas of random vortex rings [54] has a similar spectrum, the precise crossover between the k^2 and k^{-1} behaviors depending on the distribution of values of R. It is also known that in a homogeneous condensate, the kinetic-energy spectrum at very large wave numbers in the region $k_{a_0} \leqslant k \leqslant k_\xi$ scales as k^{-3} due to the presence of the singularity at the core [44].

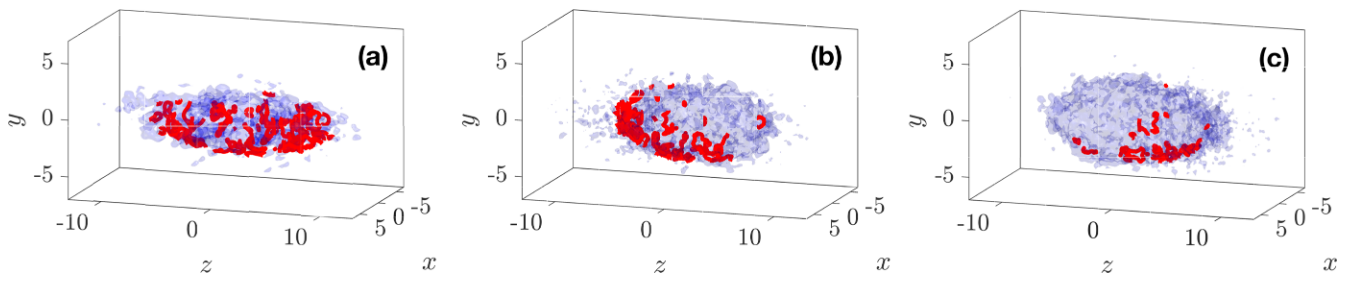

FIG. 8. The isosurfaces of the condensate (blue) with vortices marked at times (a) $t = 35.2$, (b) $t = 60.5$, and (c) $t = 92.0$.

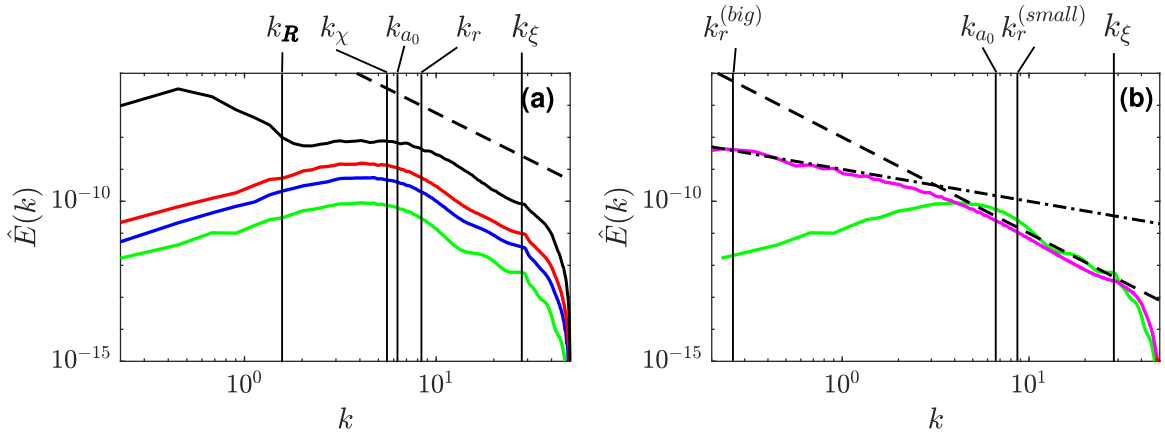

FIG. 9. The incompressible energy spectrum (a) of gas of small vortex rings; $N = 1$ (green), $N = 20$ (blue), and $N = 40$ (red) with the result of our turbulent spectra at $t = 35.2$ (black) with the wave numbers corresponding to the radial Thomas-Fermi radius, $k_{\mathbf{R}}$, the correlation length of the density fluctuations k_χ, the average width of the vortex core k_{a_0}, the radius of the average ring size, k_r, of our homogeneous system and the healing length k_ξ. The (b) $N = 1$ result is repeated (green) accompanied by the spectra of a single large ring of radii 25 (magenta) with the matching k numbers of the respective radii of the big-ring case, $k_r^{(\mathrm{big})}$, the width of the vortex core k_{a_0} and the radii of the small ring, $k_r^{(\mathrm{small})}$. The scalings $\propto k^{-3}$ (dashed) and $\propto k^{-1}$ (dot-dashed) are marked for reference.

Consider a gas of random vortex rings in a condensate. If the radii are small (of the order of the vortex core size) the region where the spectrum scales as k^{-1} disappears, and we are left with a k^{-3} spectrum at large k. We have verified this result by computing such spectrum in a homogeneous condensate [see Fig. 9(a)]. In this calculation, the rings are randomly placed within a homogeneous background, with a radius randomly, but uniformly, chosen between 4ξ and 8ξ. This range of radii is chosen to follow the radii of the vortex rings detected in our turbulent cigar condensate. The spectra of said homogeneous condensate is presented in Fig. 9(a), where the spectra for systems of $N = 1$, 20, and 40 rings is shown.

Figure 9(b) shows that the incompressible energy spectra of the turbulent condensate is very similar to the spectra of the homogeneous condensate with random rings in the large-k regime for $k > k_\chi$, where k_χ is the wave number corresponding to the correlation length of the condensate's density fluctuations χ.

This quantity is found by computing the correlation lengths χ_i $(i = x, y, z)$ of the condensate's density fluctuations in the three Cartesian planes, defined as

$$\chi_i(t) = \int_0^\infty \frac{\langle n_{fl}(\mathbf{x}, t) n_{fl}(\mathbf{x} + r_{\mathbf{i}}, t)\rangle}{\langle n_{fl}(\mathbf{x}, t)^2\rangle} dr, \tag{E1}$$

where n_{fl} is the density of the condensate with a fitted Thomas-Fermi profile removed, $n_{fl} = n - n_{TF}$, and $i = (x, y, z)$. The overall correlation is then defined as $\chi = (\chi_x + \chi_y + \chi_z)/3$. In observing Fig. 9, it clearly emerges that, for $k \geqslant k_r$ ($k_r = 2\pi/r$ with r being the average ring size for our homogeneous model) we find the same k^{-3} scaling, supporting our claim ascribing this scaling to the presence of small vortex rings in the turbulent condensate.

[1] C. F. Barenghi, L. Skrbek, and S. K. R, Introduction to quantum turbulence, Proc. Natl. Acad. Sci. USA **111**, 4647 (2014).

[2] U. Frisch, *Turbulence: The Legacy of A. N. Kolmogorov* (Cambridge University Press, Cambridge, 1995).

[3] M. LaMantia and L. Skrbek, Quantum turbulence visualized by particle dynamics, Phys. Rev. B **90**, 014519 (2014).

[4] W. Guo, S. B. Cahn, J. A. Nikkel, W. F. Vinen, and D. N. McKinsey, Visualization study of counterflow in superfluid using metastable Helium molecules, Phys. Rev. Lett. **105**, 045301 (2010).

[5] J. Maurer and P. Tabeling, Local investigation of superfluid turbulence, Europhys. Lett. **43**, 29 (1998).

[6] D. Durì, C. Baudet, J.-P. Moro, P.-E. Roche, and P. Diribarne, Hot-wire anemometry for superfluid turbulent coflows, Rev. Sci. Instrum. **86**, 025007 (2015).

[7] J. Salort, A. Monfardini, and P.-E. Roche, Micro-contilever anemometer for cryogenic helium, J. Phys.: Conf. Ser. **318**, 092030 (2011).

[8] C. F. Barenghi, V. L'vov, and P.-E. Roche, Experimental, numerical and analytical velocity spectra in turbulent quantum fluid, Proc. Natl. Acad. Sci. USA **111**, 4683 (2014).

[9] J. Salort, C. Baudet, B. Castaing, B. Chabaud, F. Daviaud, T. Didelot, P. Diribarne, B. Dubrulle, Y. Gagne, F. Gauthier *et al.*, Turbulent velocity spectra in superfluid flows, Phys. Fluids **22**, 125102 (2010).

[10] A. Kolmogorov, The Local structure of turbulence in an incompressible viscous fluid for very large Reynolds numbers, Dokl. Akad. Nauk. SSSR **30**, 301 (1941).

[11] P. M. Walmsley and A. I. Golov, Quantum and quasiclassical types of superfluid turbulence, Phys. Rev. Lett. **100**, 245301 (2008).

[12] C. F. Barenghi, Y. A. Sergeev, and A. W. Baggaley, Regimes of turbulence without an energy cascade, Sci. Rep. **6**, 35701 (2016).

[13] M. La Mantia, D. Duda, M. Rotter, and L. Skrbek, Lagrangian accelerations of particles in superfluid turbulence, J. Fluid Mech. **717**, R9 (2013).

[14] L. Galantucci and M. Sciacca, Non-classical velocity statistics in counterflow quantum turbulence, Acta Appl. Math. **132**, 273 (2014).

[15] M. T. Reeves, T. P. Billam, B. P. Anderson, and A. S. Bradley, Inverse energy cascade in forced two-dimensional quantum turbulence, Phys. Rev. Lett. **110**, 104501 (2013).

[16] G. Gauthier, M. T. Reeves, X. Yu, A. S. Bradley, M. A. Baker, T. A. Bell, H. Rubinsztein-Dunlop, M. J. Davis, and T. W. Neely, Giant vortex clusters in a two-dimensional quantum fluid, Science **364**, 1264 (2019).

[17] S. P. Johnstone, A. J. Groszek, P. T. Starkey, C. J. Billington, T. P. Simula, and K. Helmerson, Evolution of large-scale flow from turbulence in a two-dimensional superfluid, Science **364**, 1267 (2019).

[18] K. Thompson, G. Bagnato, G. Telles, M. Caracanhas, F. Dos Santos, and V. Bagnato, Evidence of power law behavior in the momentum distribution of a turbulent trapped Bose–Einstein condensate, Laser Phys. Lett. **11**, 015501 (2014).

[19] N. Navon, A. L. Gaunt, R. P. Smith, and Z. Hadzibabic, Emergence of a turbulent cascade in a quantum gas, Nature (London) **539**, 72 (2016).

[20] M. Kobayashi and M. Tsubota, Quantum turbulence in a trapped Bose–Einstein condensate, Phys. Rev. A **76**, 045603 (2007).

[21] A. C. White, C. F. Barenghi, N. P. Proukakis, A. J. Youd, and D. H. Wacks, Nonclassical velocity statistics in a turbulent atomic Bose-Einstein condensate, Phys. Rev. Lett. **104**, 075301 (2010).

[22] A. Cidrim, A. C. White, A. J. Allen, V. S. Bagnato, and C. F. Barenghi, Vinen turbulence via the decay of multicharged vortices in trapped atomic Bose–Einstein condensates, Phys. Rev. A **96**, 023617 (2017).

[23] N. G. Parker and C. S. Adams, Emergence and decay of turbulence in stirred atomic Bose-Einstein condensates, Phys. Rev. Lett. **95**, 145301 (2005).

[24] E. A. L. Henn, J. A. Seman, G. Roati, K. M. F. Magalhães, and V. S. Bagnato, Emergence of turbulence in an oscillating Bose-Einstein condensate, Phys. Rev. Lett. **103**, 045301 (2009).

[25] E. A. L. Henn, J. A. Seman, E. R. F. Ramos, M. Caracanhas, P. Castilho, E. P. Olímpio, G. Roati, D. V. Magalhães, K. M. F. Magalhães, and V. S. Bagnato, Observation of vortex formation in an oscillating trapped Bose–Einstein condensate, Phys. Rev. A **79**, 043618 (2009).

[26] J. A. Seman, E. A. L. Henn, R. F. Shiozaki, G. Roati, F. J. Poveda-Cuevas, K. M. F. Magalhães, V. I. Yukalov, M. Tsubota, M. Kobayashi, K. Kasamatsu, and V. S. Bagnato, Route to turbulence in a trapped Bose-Einstein condensate, Laser Phys. Lett. **8**, 691 (2011).

[27] J. A. Seman, E. A. L. Henn, M. Haque, R. F. Shiozaki, E. R. F. Ramos, M. Caracanhas, P. Castilho, C. Castelo Branco, P. E. S. Tavares, F. J. Poveda-Cuevas, G. Roati, K. M. F. Magalhães, and V. S. Bagnato, Three-vortex configurations in trapped Bose-Einstein condensates, Phys. Rev. A **82**, 033616 (2010).

[28] A. Daniel García-Orozco, L. Madeira, L. Galantucci, C. F. Barenghi, and V. S. Bagnato, Intra-scales energy transfer during the evolution of turbulence in a trapped Bose-Einstein condensate, Europhys. Lett. **130**, 46001 (2020).

[29] A. Bahrami, P. Tavares, A. Fritsch, Y. Tonin, G. Telles, V. Bagnato, and E. Henn, Investigation of the momentum distribution of an excited bec by free expansion: Coupling with collective modes, J. Low Temp. Phys. **180**, 126 (2015).

[30] A. D. García-Orozco, L. Madeira, M. A. Moreno-Armijos, A. R. Fritsch, P. E. S. Tavares, P. C. M. Castilho, A. Cidrim, G. Roati, and V. S. Bagnato, Universal dynamics of a turbulent superfluid Bose gas, Phys. Rev. A **106**, 023314 (2022).

[31] R. Shiozaki, G. Telles, V. Yukalov, and V. Bagnato, Transition to quantum turbulence in finite-size superfluids, Laser Phys. Lett. **8**, 393 (2011).

[32] R. Desbuquois, L. Chomaz, T. Yefsah, J. Leonard, J. Beugnon, C. Weitenberg, and J. Dalibard, Superfluid behaviour of a two-dimensional Bose gas, Nat. Phys. **8**, 645 (2012).

[33] W. Kwon, G. Del Pace, K. Xhani, L. Galantucci, A. Muzi Falconi, M. Inguscio, F. Scazza, and G. Roati, Sound emission and annihilations in a programmable quantum vortex collider, Nature (London) **600**, 64 (2021).

[34] D. Frantzeskakis, Dark solitons in atomic Bose–Einstein condensates: From theory to experiments, J. Phys. A: Math. Theor. **43**, 213001 (2010).

[35] M. Mossman, M. Hoefer, K. Julien, P. Kevrekidis, and P. Peter Engels, Dissipative shock waves generated by a quantum-mechanical piston, Nat. Commun. **9**, 4665 (2018).

[36] C. Rorai, J. Skipper, R. M. Kerr, and K. R. Sreenivasan, Approach and separation of quantised vortices with balanced cores, J. Fluid Mech. **808**, 641 (2016).

[37] A. Villois, G. Krstulovic, D. Proment, and H. Salman, A vortex filament tracking method for the Gross–Pitaevskii model of a superfluid, J. Phys. A: Math. Theor. **49**, 415502 (2016).

[38] S. Serafini, L. Galantucci, E. Iseni, T. Bienaimé, R. N. Bisset, C. F. Barenghi, F. Dalfovo, G. Lamporesi, and G. Ferrari, Vortex reconnections and rebounds in trapped atomic Bose-Einstein condensates, Phys. Rev. X **7**, 021031 (2017).

[39] P. Rosenbusch, V. Bretin, and J. Dalibard, Dynamics of a single vortex line in a Bose-Einstein condensate, Phys. Rev. Lett. **89**, 200403 (2002).

[40] M. Modugno, L. Pricoupenko, and Y. Castin, Bose-Einstein condensates with a bent vortex in rotating traps, Eur. Phys. J. D **22**, 235 (2003).

[41] S. Komineas, N. R. Cooper, and N. Papanicolaou, Single vortex states in a confined Bose-Einstein condensate, Phys. Rev. A **72**, 053624 (2005).

[42] S. Serafini, M. Barbiero, M. Debortoli, S. Donadello, F. Larcher, F. Dalfovo, G. Lamporesi, and G. Ferrari, Dynamics and interaction of vortex lines in an elongated Bose-Einstein condensate, Phys. Rev. Lett. **115**, 170402 (2015).

[43] B. Rousset, P. Bonnay, P. Diribarne, A. Girard, J. M. Poncet, E. Herbert, J. Salort, C. Baudet, B. Castaing, L. Chevillard, F. Daviaut, B. Dubrulle, Y. Gagne, M. Gibert, B. Hebral, T. Lehner, P.-E. Roche, B. Saint-Michel, and M. Bon Mardion, Superfluid high Reynolds von Kármán experiment, Rev. Sci. Instrum. **85**, 103908 (2014).

[44] C. Nore, M. Abid, and M. Brachet, Decaying Kolmogorov turbulence in a model of superflow, Phys. Fluids **9**, 2644 (1997).

[45] M. R. Smith, R. J. Donnelly, N. Goldenfeld, and W. F. Vinen, Decay of vorticity in homogeneous turbulence, Phys. Rev. Lett. **71**, 2583 (1993).

[46] S. R. Stalp, L. Skrbek, and R. J. Donnelly, Decay of grid turbulence in a finite channel, Phys. Rev. Lett. **82**, 4831 (1999).

[47] W. Vinen and J. Niemela, Quantum turbulence, J. Low Temp. Phys. **128**, 167 (2002).

[48] S. Nazarenko, Wave turbulence, Contemp. Phys. **56**, 359 (2015).

[49] V. L'vov and S. Nazarenko, Weak turbulence of Kelvin waves in superfluid He, Low Temp. Phys. **36**, 785 (2010).

[50] G. Krstulovic, Kelvin-wave cascade and dissipation in low-temperature superfluid vortices, Phys. Rev. E **86**, 055301(R) (2012).

[51] S. Nazarenko and M. Onorato, Wave turbulence and vortices in Bose-Einstein condensation, Phys. D (Amsterdam, Neth.) **219**, 1 (2006).

[52] https://doi.org/10.25405/data.ncl.24282595.

[53] A. Leonard, Computing three-dimensional incompressible flows with vortex elements, Annu. Rev. Fluid Mech. **17**, 523 (1985).

[54] O. Yurkina and S. Nemirovskii, On the energy spectrum of the 3D velocity field, generated by an ensemble of vortex loops, Low Temp. Phys. **47**, 652 (2021).